J. Fluid Mech. (2013), *vol.* 717, *pp.* 166–192.
doi:10.1017/jfm.2012.565

Reynolds number and aspect ratio effects on the leading-edge vortex for rotating insect wing planforms

R. R. Harbig†, J. Sheridan and M. C. Thompson

Fluids Laboratory for Aeronautical and Industrial Research (FLAIR), Department of Mechanical and Aerospace Engineering, Monash University, Clayton, VIC 3800, Australia

(Received 21 June 2012; revised 20 September 2012; accepted 13 November 2012; first published online 1 February 2013)

Previous studies investigating the effect of aspect ratio (*AR*) for insect-like regimes have reported seemingly different trends in aerodynamic forces, however no detailed flow observations have been made. In this study, the effect of *AR* and Reynolds number on the flow structures over insect-like wings is explored using a numerical model of an altered fruit fly wing revolving at a constant angular velocity. Increasing the Reynolds number for an *AR* of 2.91 resulted in the development of a dual leading-edge vortex (LEV) structure, however increasing *AR* at a fixed Reynolds number generated the same flow structures. This result shows that the effects of Reynolds number and *AR* are linked. We present an alternative scaling using wing span as the characteristic length to decouple the effects of Reynolds number from those of *AR*. This results in a span-based Reynolds number, which can be used to independently describe the development of the LEV. Indeed, universal behaviour was found for various parameters using this scaling. The effect of *AR* on the vortex structures and aerodynamic forces was then assessed at different span-based Reynolds numbers. Scaling the flow using the wing span was found to apply when a strong spanwise velocity is present on the leeward side of the wing and therefore may prove to be useful for similar studies involving flapping or rotating wings at high angles of attack.

Key words: biological fluid dynamics, swimming/flying

1. Introduction

Many current micro-air vehicle (MAV) designs have been inspired by nature as MAV designers wish to match the aerodynamic manoeuvrability, efficiency and stability of insects and small birds. Despite some progress, the performance of these MAVs is still inferior to that of natural flyers (Pines & Bohorquez). In order to bridge this gap in flight performance, further advances in our understanding of the aerodynamics of flapping and rotating wings is required.

Research into the aerodynamics of insect flight has shown that the presence of a stable leading-edge vortex (LEV) provides insect wings with additional circulation and enhanced lift during hovering flight (Ellington *et al.* ; Usherwood & Ellington ; Birch, Dickson & Dickinson). This persistent LEV is a common occurrence in the insect world, and it has been observed for many species of

† Email address for correspondence: robert.harbig@monash.edu

insects (e.g. Ellington *et al.* ; Srygley & Thomas ; Liu & Aono). Studies investigating the velocity field around flapping wings have shown the three-dimensional structure of the LEV and have highlighted the presence of strong spanwise flow from wing root to tip (Birch & Dickinson ; Birch *et al.* ; Poelma, Dickson & Dickinson). Lentink & Dickinson ( ) suggest that it is the propeller-like rotation of the wing that stabilizes the LEV to the wing's surface, although Jones & Babinsky (,) have observed unstable LEVs in their semi-submersed waving wing experiments.

Despite the variety of wing shapes seen in nature, seemingly little work has been aimed at understanding the effect that wing geometry has on the optimal aerodynamic performance of these insects. One critical wing design parameter for large aircraft is wing aspect ratio (*AR*), however the effect of this parameter for flapping and rotating wings in insect-like flight regimes is not well understood. Noticeably, different insects have different wing aspect ratios and often seemingly contradictory results have been reported in the literature. In some cases, little change in forces has been observed (Usherwood & Ellington ; Luo & Sun), whilst in others there have been clear trends (Tsuzuki, Sato & Abe ; Ansari, Knowles & Zbikowski). Indeed, it is still unclear whether *AR* is a significant design parameter for optimal aerodynamic performance in insect flight.

Furthermore, no observations have been made to highlight potential changes in the LEV's structure with *AR* and to link these changes to the aerodynamic forces. It has been suggested that it is the centripetal and Coriolis accelerations resulting from the low-Rossby-number rotation that are required for LEV stability, and that the Rossby number (*Ro*) is equal to the wing's *AR* for hovering flight (Lentink & Dickinson). This suggests that there should indeed be a change in the LEV's characteristics with *AR* as low-aspect-ratio wings would be required for the LEV to be stable. However, the manner in which the LEV structure changes with *AR* is unknown.

This paper describes an investigation into the effect of *AR* on rotating wings at insect Reynolds numbers. A numerical model of a fruit fly wing undergoing constant velocity rotation is first presented and the change in the structure of the LEV with Reynolds number is highlighted. This model is then extended to different *AR* wings and analysis of the vortex structures reveals that *AR* has the same effect as the Reynolds number on the LEV. An alternate scaling parameter is presented that decouples the effect of *AR* and Reynolds number. Finally, the applications to which this new scaling parameter can be applied are explored.

2. Numerical method

The flow over a revolving wing is modelled by the Navier–Stokes equations cast in a non-inertial rotating frame of reference and combined with the continuity constraint,

$$\frac{\partial \rho \boldsymbol{u}_{abs}}{\partial t} + \boldsymbol{\nabla} \cdot (\rho \boldsymbol{u}\boldsymbol{u}_{abs}) = -\boldsymbol{\nabla} p + \boldsymbol{\nabla} \cdot \boldsymbol{\tau} - \rho \boldsymbol{\Omega} \times \boldsymbol{u} - \rho \boldsymbol{\Omega} \times (\boldsymbol{\Omega} \times \boldsymbol{r}), \tag{2.1}$$

and

$$\boldsymbol{\nabla} \cdot \boldsymbol{u} = 0. \tag{2.2}$$

Here ρ is the fluid density, $\boldsymbol{u}$ and $\boldsymbol{u}_{abs}$ are the velocity vectors in rotating and absolute frames, respectively, p is the pressure, $\boldsymbol{\Omega}$ is the rotational velocity vector, $\boldsymbol{r}$ is the location vector and $\boldsymbol{\tau}$ is the stress tensor, which is defined as

$$\boldsymbol{\tau} = \mu(\boldsymbol{\nabla u} + (\boldsymbol{\nabla u})^{\mathrm{T}} - \tfrac{2}{3}\boldsymbol{I}\boldsymbol{\nabla} \cdot \boldsymbol{u}), \tag{2.3}$$

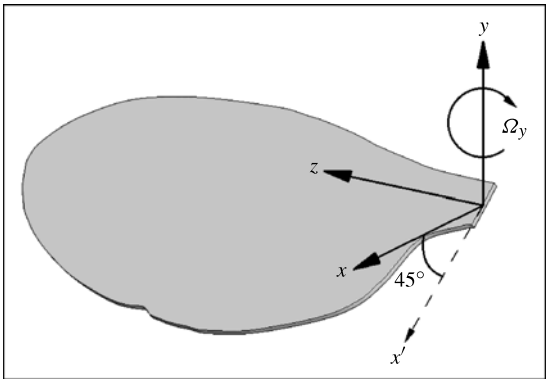

FIGURE 1. Schematic of the fly wing geometry and coordinate system.

where μ is the fluid viscosity and $\boldsymbol{I}$ is the identity matrix. The last two terms in (2.1) are the Coriolis and centrifugal momentum source terms due to the rotating frame. In order to minimize numerical error an alternate rotation model was used whereby the velocity in the advection and transient terms is modified to involve the absolute frame velocity rather than the relative frame velocity, hence the use of $\boldsymbol{u}_{abs}$ in (2.1). The angular acceleration of the fluid is included in the transient term as $\boldsymbol{u}_{abs} = \boldsymbol{u} + \boldsymbol{\Omega} \times \boldsymbol{r}$. These equations were solved directly using the commercial finite-volume-based code ANSYS CFX. The formally second-order accurate specified blend factor scheme (with $\beta = 1$) was used for spatial discretization along with a second-order backward Euler scheme for the time evolution terms.

The wing planform shape used in this study was based on a generic fruit fly wing (*Drosophila melanogaster*). This planform was chosen as it has been studied extensively both computationally (Liu & Aono ; Kweon & Choi) and experimentally (Birch & Dickinson ; Birch *et al.* ; Poelma *et al.* ; Lentink & Dickinson). The wing was modelled as a rigid flat plate with square edges with a thickness of 3 % of the mean chord. A schematic of the fruit fly wing geometry and the coordinate system used in the computation is shown in figure . Initially the wing was scaled to have a wing span of 2.47 mm and an *AR* of 2.91, similar to that of an actual fly's wing (Zanker & Gotz). This wing shape was then stretched to produce wings of different aspect ratios to reflect the variety seen in nature (for examples see Ellington ; Shyy *et al.*).

A simplified kinematic motion was prescribed for the wing to simulate the vortex structures that are formed during the mid-stroke of a typical insect flapping cycle without the complication of wing rotation and reversal. The kinematic motion consisted only of a rotation about the wing's base at a constant angle of attack of 45°. The wing was initially at rest and was accelerated over a period of $t = 0.084T$ before rotating at a constant rotational velocity Ω. An impulsively started wing rotating about its base has been shown to be a good approximation to the beginning of the down stroke of a typical insect flapping cycle (Poelma *et al.* ; Lentink & Dickinson) where the acceleration period typically ranges between 6 and 10 % of the overall simulation time (Dickinson, Lehmann & Sane ; Birch *et al.* ; Lentink & Dickinson). This kinematic motion is described by (2.4) where T is the total

			$Re = 120$				$Re = 1500$			
Mesh	Surface size	Elements (million)	C_L	GCI (%)	C_D	GCI (%)	C_L	GCI (%)	C_D	GCI (%)
1	$0.02857\bar{c}$	1.538	1.540	—	1.620	—	1.835	—	1.720	—
2	$0.01449\bar{c}$	5.490	1.543	0.251	1.609	0.066	1.842	0.546	1.704	0.564
3	$0.00725\bar{c}$	27.36	1.545	0.094	1.608	0.002	1.837	0.258	1.698	0.134

TABLE 1. Mesh resolution study.

simulation time,

$$\Omega_y(t) = \begin{cases} \frac{1}{2}\Omega\left(1 - \cos\left(\frac{\pi t}{0.084T}\right)\right), & t < 0.084T \\ \Omega, & t \geqslant 0.084T. \end{cases} \tag{2.4}$$

The simulation was stopped after the wing had completed 270° of rotation. As will be shown in § 3.2 this allowed ample time for a quasi-steady flow state to form. The Reynolds number (Re) was calculated using the velocity at the radius of gyration (U_{rg}) and the mean chord length. Similarly, the lift and drag coefficients were calculated as $C_L = 2L/\rho U_{rg}^2 S$ and $C_D = 2D/\rho U_{rg}^2 S$, respectively, where S is the wing area. Altering the wing's aspect ratio either by chord or by span also varies the Reynolds number. Changing the wing's span alters U_{rg} as the radius of gyration is altered, and changing the wing's chord directly affects the Reynolds number. Therefore, the fluid viscosity was adjusted to maintain a constant Reynolds number for each AR wing.

The wing was located in the centre of a cylindrically shaped computational domain whose axis was coincident with the rotation axis of the wing, whose diameter was 18 times the wing span, and whose length was 48 times the average wing chord. The boundary condition on the outer cylindrical surface was a free-slip wall condition ($U_n = 0$), while for the top and bottom circular surfaces fluid was allowed to flow into and out of the domain with the average pressure on each boundary held at zero gauge pressure. A no-slip boundary condition was applied at the wing's surface.

The computational domain was meshed using an unstructured tetrahedral mesh with a region of triangular prism elements near the wing's surface. To explore spatial resolution effects, three grids were generated such that the element size on the wing's surface and in the surrounding fluid zones were successively halved. The calculated aerodynamic force coefficients are shown in table for each mesh at Reynolds numbers of 120 and 1500. The *grid convergence index* (GCI) method was used to estimate the numerical error (Roache). Mesh 2 had a GCI of less than 0.6 % and was determined to be adequate. The temporal error was estimated in a similar way and was found to have a GCI of 0.15 % for C_L and C_D with a time step of $0.00185T$.

3. Results and discussion

3.1. *Reynolds number effects for a fly wing*

Simulations of the fruit fly wing ($AR = 2.91$) at various Reynolds numbers were used to validate the numerical model against similar experimental investigations. Results at Reynolds numbers of 120 (fruit fly scale) and 1500 (house fly or bee scale) were used to compare to the air bubble flow visualizations of Lentink & Dickinson ( ). To visualize the flow features in a similar manner, a particle tracking model was used to model the behaviour of neutrally buoyant particles ejected along the leading

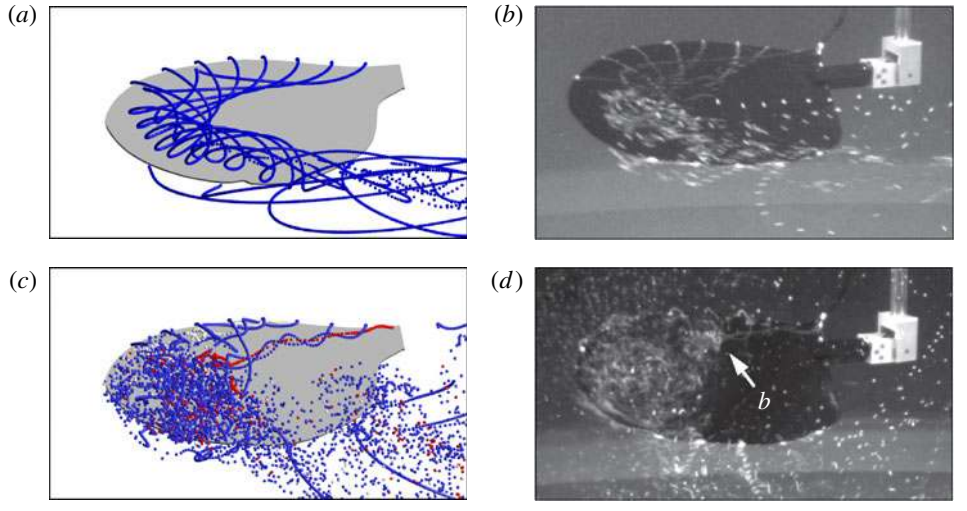

FIGURE 2. (Colour online) Comparison of numerical particle tracking flow visualization results at (*a*) $Re = 120$ and (*c*) $Re = 1500$ with air bubble flow visualizations of Lentink & Dickinson ( ) (reproduced with permission) at (*b*) $Re = 110$ and (*d*) $Re = 1400$.

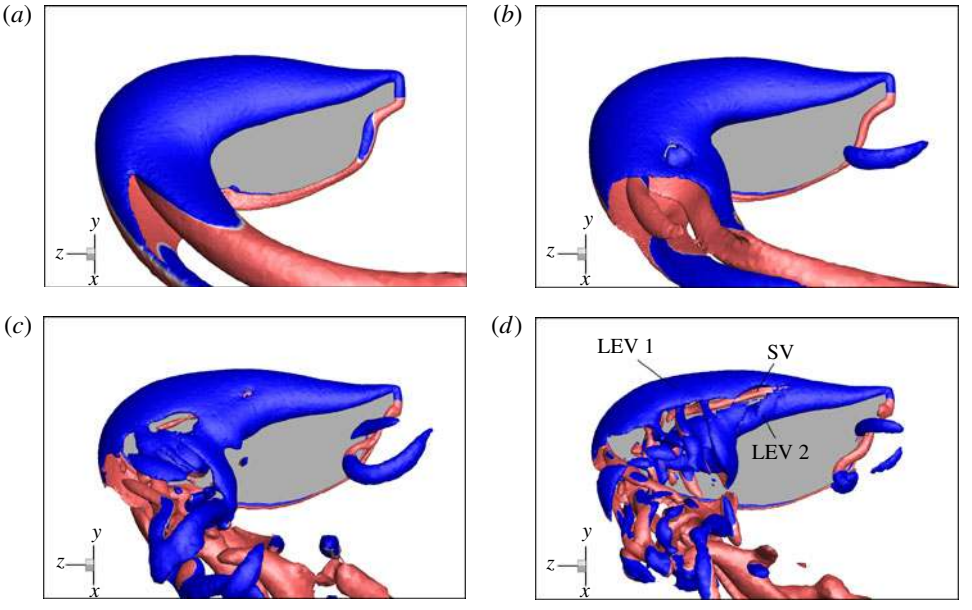

FIGURE 3. (Colour online) Development of vortex structures over a fruit fly wing ($AR = 2.91$) with Reynolds number (*a*) $Re = 120$, (*b*) $Re = 300$, (*c*) $Re = 750$ and (*d*) $Re = 1500$. Vortex structures are visualized using surfaces of constant Q criterion and are coloured by spanwise vorticity (ω_z) to indicate direction; blue (dark grey) is negative and red (light grey) is positive. Images show the instantaneous flow structures at 270° of rotation and are taken perpendicular to the wing surface.

and trailing edges of the wing. These results are compared in figure and show good agreement with the experimental visualizations at both Reynolds numbers. At a Reynolds number of 120 the LEV does not form a tight spiral (as for the higher-Reynolds-number cases) and is attached to the wing along its span to approximately the 70 % span position, at which point it joins with the tip vortex as it separates from the wing. Figure (*a*) shows a more detailed view of the vortex structures at this Reynolds number and shows that the LEV grows in size in the spanwise direction. In addition, the trailing-edge vortex separates from the wing slightly closer to the wing tip, thus forming a pair of counter-rotating vortices in the wake. This vortex structure was also observed by Poelma *et al.* ( ) in their particle image velocimetry experiments on a flapping fruit fly wing.

At a Reynolds number of 1500, figure (*c*) and (*d*) show a tight spiral LEV which breaks down at approximately 60 % span, resulting in an unsteady region of flow near the wing tip. Figure (*c*) also shows a second vortex structure closer to the leading-edge which is not seen in figure (*d*), however this dual LEV system was observed by Lentink & Dickinson ( ) towards the end of the wing's stroke at a Reynolds number of 1400. A dual leading-edge vortex structure has been observed by Srygley & Thomas ( ) over butterfly wings during wing beats that resulted in very large accelerations of the butterfly and has been shown to exist under certain Reynolds number conditions and angles of attack for a range of wing shapes (Lu, Shen & Lai ; Phillips, Knowles & Lawson).

Figure shows the development of this dual LEV structure with Reynolds number, where the vortices are visualized using surfaces of constant Q criterion. The Q value is the second invariant of the velocity gradient tensor (Hunt, Wray & Moin) and is a measure of the magnitude of rotation rate relative to strain rate in a fluid. Positive values of Q represent areas where the local magnitude of rotation in the fluid dominates relative to strain and therefore can be used to highlight vortical structures. Figure shows that as the Reynolds number increases, the iso-Q surfaces near the leading edge split, resulting in two co-rotating vortex structures (labelled LEV 1 and 2) separated by a smaller counter-rotating vortex (labelled SV). At high Reynolds numbers the vortex structure furthest away from the leading edge of the wing (LEV 2) breaks down near to the wing tip.

The development of this dual vortex structure with Reynolds number is further highlighted in figure , which shows the change in spanwise vorticity patterns at 50 % span. At a Reynolds number of 120 a single region of strong negative (blue/dark grey) vorticity is located near the leading-edge of the wing. As the Reynolds number is increased a region of negative vorticity develops further downstream of the leading edge near to the wing's surface. At first ($Re = 300$) these two regions of negative vorticity are merged together forming a large region of vorticity near the leading edge. As the Reynolds number is increased further ($Re = 750$ and 1500) the strength of the vorticity in the region furthest downstream of the leading edge increases and the two regions split to form two distinct vortex cores. As this dual vortex structure forms, the proximity of LEV 2 to the wing's surface induces a flow near the wall. When the Reynolds number is increased and the strength of LEV 2 increases, this boundary layer separates due to the adverse pressure gradient generated by LEV 2 and forms a secondary region of positive vorticity between the two regions of negative vorticity. The formation of this counter-rotating vortex is similar to the vortex structure that forms for a vortex ring impacting a wall (Walker *et al.*). Furthermore, the overall change in vorticity pattern with Reynolds number is very similar to that observed by Lu *et al.* ( ) for an $AR = 5.8$ flapping wing at 60° angle of attack.

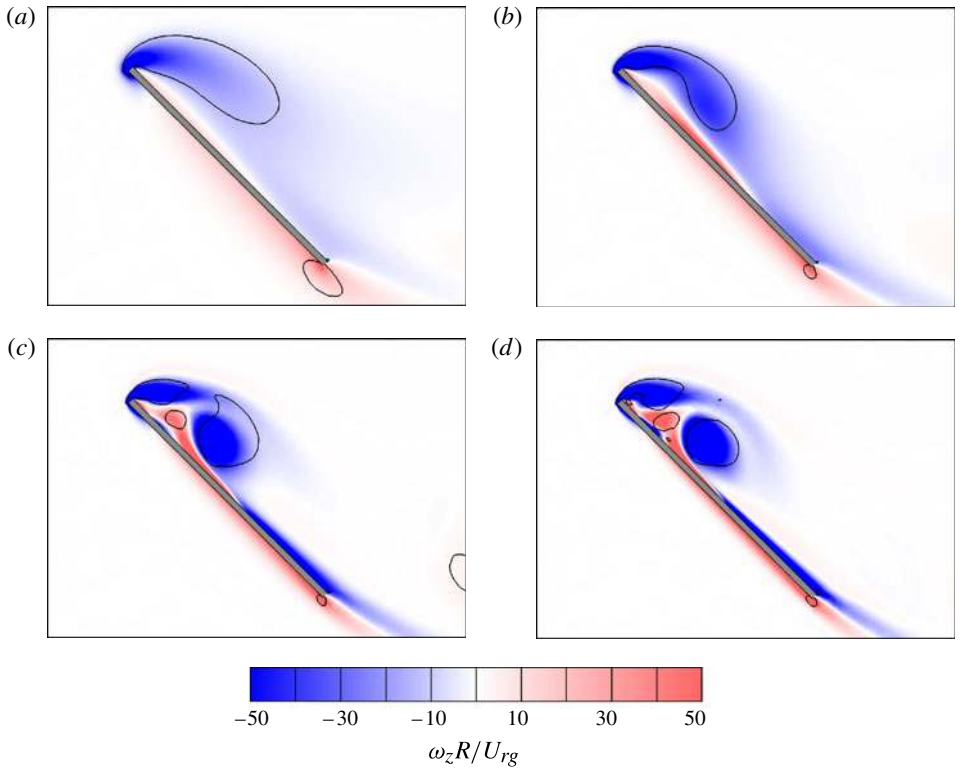

FIGURE 4. (Colour online) Contours of spanwise vorticity ($\omega_z R/U_{rg}$) at 50 % span for Reynolds numbers of (*a*) 120, (*b*) 300, (*c*) 750 and (*d*) 1500. Solid lines are contours of constant Q criterion. Images show the instantaneous flow structures at 270° of rotation.

The vortex centre identification algorithm presented by Graftieaux, Michard & Grosjean ( ) was employed to calculate the location of the LEV axis at various spanwise locations. This method calculates a scalar field, γ_1, which is a measure of the relative rotation about each grid point constrained to a definable interrogation window. The discrete scalar function is defined as

$$\gamma_1(P) = \frac{1}{N}\sum_M \frac{(\boldsymbol{R}_{PM} \wedge \boldsymbol{U}_M)\cdot \boldsymbol{z}}{\|\boldsymbol{R}_{PM}\| \cdot \|\boldsymbol{U}_M\|} = \frac{1}{N}\sum_M \sin(\theta_M), \tag{3.1}$$

where N is the number of grid points, M, within a bounded square region centred on grid point P. γ_1 is equivalent to the ensemble average of $\sin(\theta_M)$, where θ_M represents the angle between the velocity vector $\boldsymbol{U}_M$ and the radius vector $\boldsymbol{R}_{PM}$. The magnitude of γ_1 is bounded by one and is calculated on two-dimensional (2D) velocity planes in the chordwise direction, where $\boldsymbol{z}$ is the unit normal vector of the plane. The centre of a vortex core is identified as a local maximum of the $|\gamma_1|$ field. The location of each of the vortex centres across the span are plotted in figure (*a*) and highlight that the position of the dual vortex structure is independent of Reynolds number. LEV 1 largely follows the shape of the leading edge, only deviating slightly as the spanwise position increases, while LEV 2 moves away from the leading edge as it tracks across the wing.

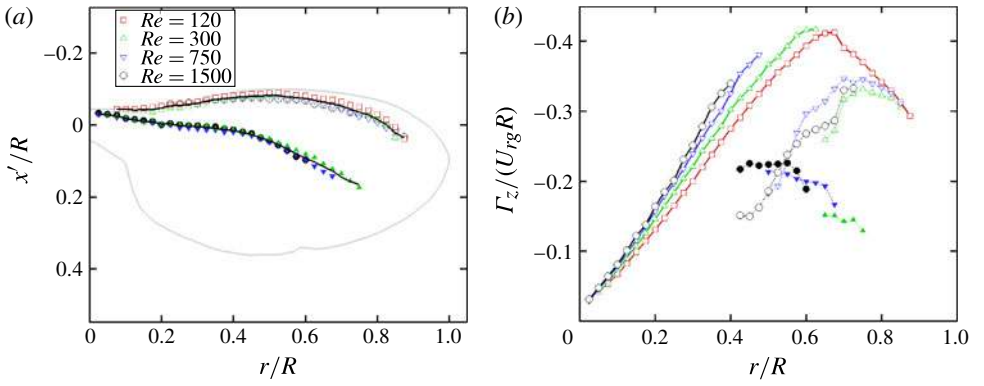

FIGURE 5. (Colour online) LEV plots of an $AR = 2.91$ wing at various Reynolds numbers: (*a*) position of the vortex axis plotted in wing coordinates; and (*b*) the circulation ($\Gamma_z/U_{rg}R$) of the co-rotating vortices. Solid black lines in (*a*) are the average vortex positions and the grey line is the wing outline. Solid lines in (*b*) represent regions where vortex cores are merged and therefore are the combined circulation of the dual co-rotating vortices. Dotted lines show the circulation of the individual vortices after they have split. For both figures, open symbols are LEV 1 and filled symbols are LEV 2.

The circulation of the dual vortex structure was calculated using the Graftieaux *et al.* ( ) vortex core identification algorithm, in which the previously defined scalar field is modified to take into account the local advection velocity $\boldsymbol{U}_P$ around P. The new field is

$$\gamma_2(P) = \frac{1}{N}\sum_M \frac{[\boldsymbol{R}_{PM} \wedge (\boldsymbol{U}_M - \boldsymbol{U}_P)] \cdot \boldsymbol{z}}{\|\boldsymbol{R}_{PM}\| \cdot \|\boldsymbol{U}_M - \boldsymbol{U}_P\|}, \tag{3.2}$$

where $|\gamma_2|$ is again bounded by one. Regions where $|\gamma_2| > 2/\pi$ are locally dominated by rotation and therefore represent a vortex core. The spanwise vorticity within these regions was integrated to calculate the circulation of the dual LEV system which is plotted in figure (*b*). The solid lines represent regions where the two vortex cores are merged together and therefore represents the combined circulation of the dual co-rotating vortices. Dotted lines show the circulation of the individual vortices after they have split. Figure (*b*) shows that the combined circulation initially increases approximately linearly with span. Except for a Reynolds number of 120, where only LEV 1 is present, the two vortex cores split at some point along the span and this point moves towards the wing root with increasing Reynolds number. After the split, the circulation of LEV 2 is fairly constant with span until it breaks down, which indicates that after the two vortex cores separate, vorticity is no longer fed into the second vortex. The circulation of LEV 1 continues to grow approximately linearly with span after the split up to ∼70 % span.

The spanwise velocity distribution over the wing is also influenced by Reynolds number. Birch *et al.* ( ) found that an increase in Reynolds number caused the peak in the spanwise velocity to strengthen and shift to be within the core of the LEV. The development of the spanwise velocity with Reynolds number for our simulations is shown in figure . At a Reynolds number of 120, a broad region of positive (root to tip) spanwise flow extends across the wing. While there is some positive velocity within the core of the LEV the maximum spanwise flow is located behind the LEV.

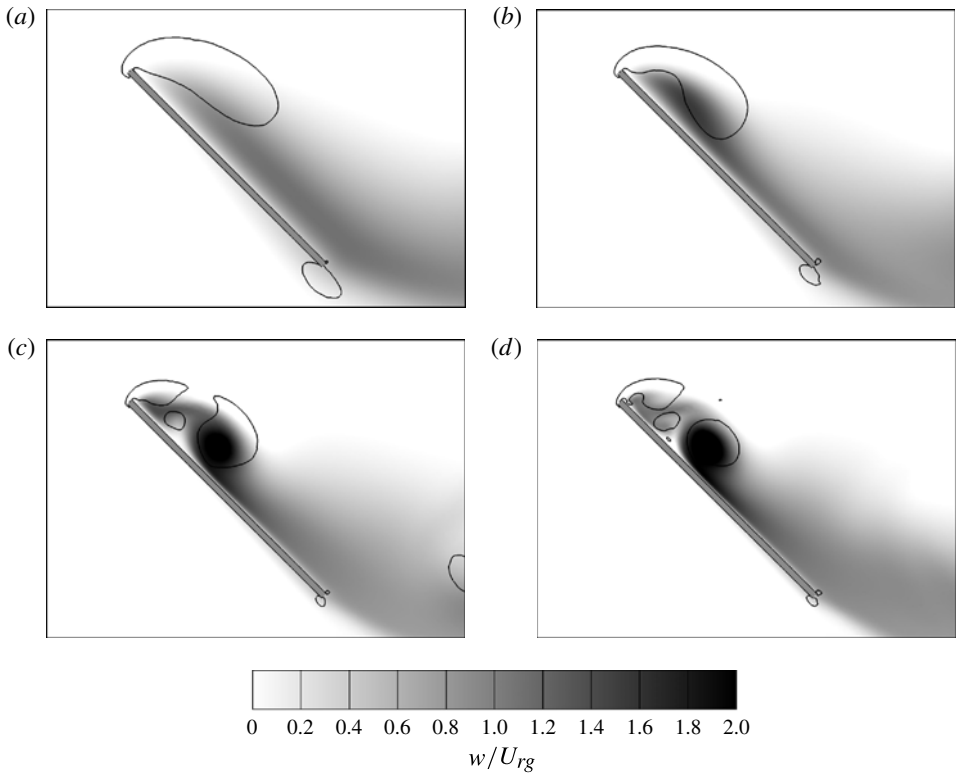

FIGURE 6. Contours of spanwise velocity (w/U_{rg}) at 50 % span for Reynolds numbers of (*a*) 120, (*b*) 300, (*c*) 750 and (*d*) 1500. Solid lines are contours of constant Q criterion. Images show the instantaneous velocity fields at 270° of rotation.

This spanwise velocity pattern is similar to those observed by Birch *et al.* ( ) and Poelma *et al.* ( ). As the Reynolds number increases, and the dual vortex structure develops, the spanwise velocity increases within the core of the downstream vortex (LEV 2) such that the peak in spanwise velocity shifts to be within LEV 2. At high Reynolds numbers there is still significant spanwise velocity in the region behind the LEV system, however the spanwise flow within the core of LEV 1 is relatively weak.

3.2. *Temporal development of flow structures*

In this section the variation of the aerodynamic forces and flow structures throughout the wing's motion are described. An example of the change in lift coefficient with time is compared with the experimental force measurements of Birch *et al.* ( ) in figure . Here, it should be noted that the current computational fluid dynamics (CFD) model is not intended to be an exact replica of their experiment. Nonetheless, the variation of the aerodynamic force is consistent with previously reported aerodynamic forces for impulsively started rotating wings (Dickinson *et al.* ; Birch *et al.*), where there is an initial transient period in which the lift coefficient reaches a maximum, which is followed by a lift minimum, before the lift coefficient recovers and there is a period of approximately constant force production. The average lift coefficient is approximately 9 % lower than the average measured lift coefficient for both Reynolds numbers, while the maximum lift coefficient is 12 and 18 % lower for

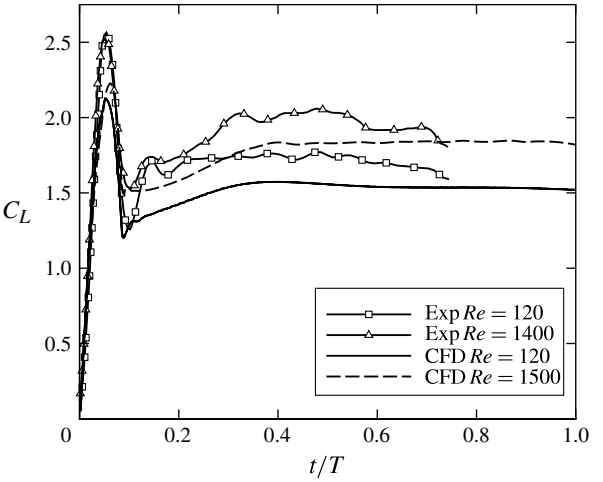

FIGURE 7. Lift coefficient time history for an $AR = 2.91$ wing compared with the experimental results of Birch *et al.* ( ).

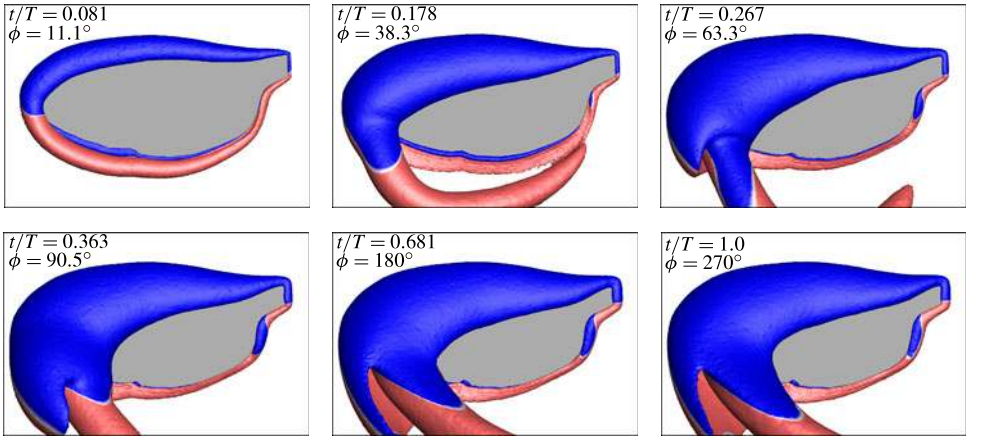

FIGURE 8. (Colour online) Temporal vortex structure development over a fruit fly wing ($AR = 2.91$) at $Re = 120$. Vortex structures are visualized using surfaces of constant Q criterion and are coloured by spanwise vorticity (ω_z) to indicate direction; blue (dark grey) is negative and red (light grey) is positive. Images show the instantaneous flow structures throughout the wing's rotation and are taken perpendicular to the wing surface.

the high and low Reynolds numbers, respectively. The large steady lift coefficients that are produced after the initial transient period indicate that a quasi-steady flow regime has developed where the LEV remains attached to the wing. To explore this further, the development of the vortex structures near the wing's surface at six time instances throughout the simulation are shown in figures and .

Figure shows the iso-Q surfaces during the wing's motion for a Reynolds number of 120. At the beginning of the wing's motion, a horseshoe-shaped vortex is formed which consists of the LEV, tip vortex and trailing-edge vortex. As the wing continues to rotate, this vortex grows in size and the trailing-edge vortex is shed from the

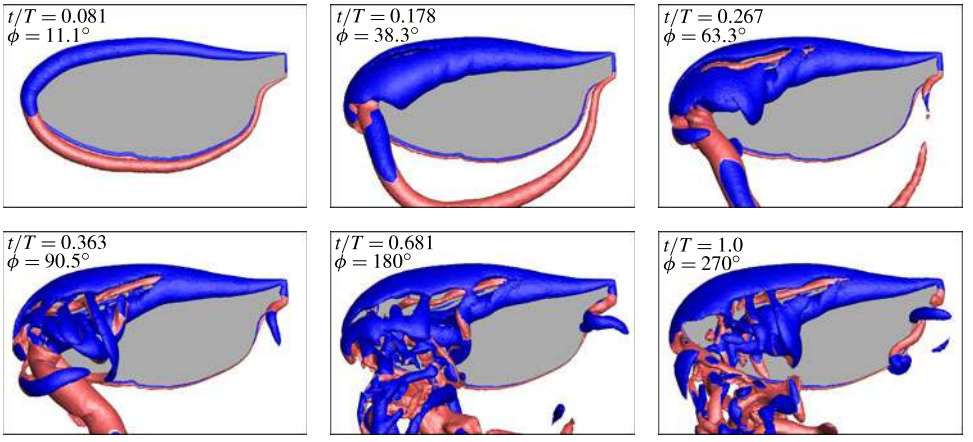

FIGURE 9. (Colour online) Temporal vortex structure development over a fruit fly wing ($AR = 2.91$) at $Re = 1500$. Vortex structures are visualized using surfaces of constant Q criterion and are coloured by spanwise vorticity (ω_z) to indicate direction; blue (dark grey) is negative and red (light grey) is positive. Images show the instantaneous flow structures throughout the wing's rotation and are taken perpendicular to the wing surface.

wing. Noticeably, the LEV enlarges towards the wing tip which results in a three-dimensional (3D) vortex structure. This flow structure development is similar to that computed for the initial part of the downstroke of a hovering fruit fly (Aono, Liang & Liu). At $t/T = 0.267$ a second trailing-edge vortex can be seen to detach from the wing on the wing tip side of the tip vortex. By $t/T = 0.363$ the growth of the LEV has stopped and the structure of the LEV remains steady for the rest of the simulation. The second trailing-edge vortex continues to develop in the wake, forming a counter-rotating vortex pair with the tip vortex, however this does not have a significant impact on the aerodynamic forces.

The development of the vortex structures at a Reynolds number of 1500 is shown in figure . Initially, a similar horseshoe-shaped vortex structure is formed as was seen at a Reynolds number of 120. At $t/T = 0.178$ the trailing-edge vortex also separates from the wing in a similar manner, however here the iso-Q surface representing the LEV begins to split near the tip of the wing. By $t/T = 0.267$ a clear dual LEV structure has formed and by $t/T = 0.363$ LEV 2 has burst, resulting in smaller-scale structures forming. These smaller-scale structures are advected into the wake as the wing's motion continues, however the LEV structure appears to be fully developed and consistent in size and position from $t/T = 0.363$.

As is shown by both the lift coefficient time history (figure) and the vortex structure development (figures and), a quasi-steady flow state has developed for the vortex structures immediately near the wing by approximately $t/T = 0.36$, or 90° of wing rotation. This period of flow development is similar to that reported by Poelma *et al.* ( ).

3.3. *Effect of AR at constant Reynolds number*

The fruit fly wing simulation at a Reynolds number of 300 was used as the basis for an initial investigation into the effect of AR. The wing was scaled to create wings of different aspect ratios while the fluid viscosity was adjusted to maintain a constant

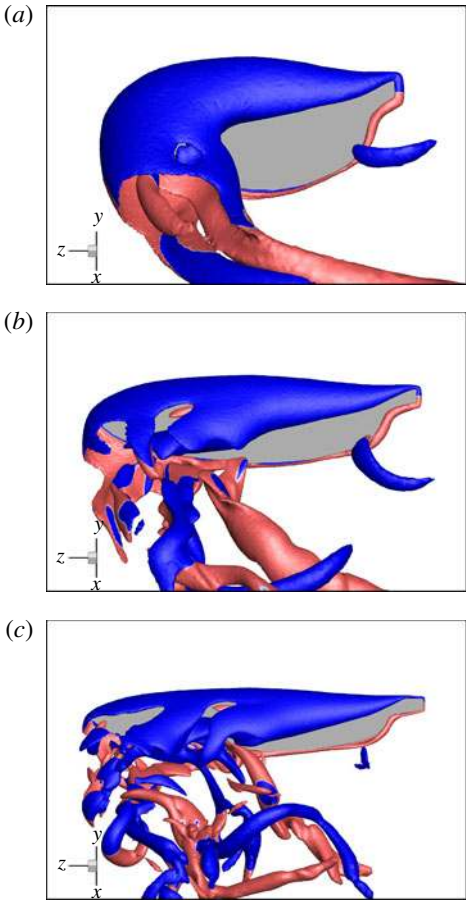

FIGURE 10. (Colour online) Variation of the vortex structures for different AR wings at $Re = 300$: (*a*) $AR = 2.91$; (*b*) $AR = 5.1$; (*c*) $AR = 7.28$. Vortex structures are visualized using surfaces of constant Q criterion and are coloured by spanwise vorticity (ω_z) to indicate direction; blue (dark grey) is negative and red (light grey) is positive. Images show the instantaneous flow structures at 270° of rotation and are taken perpendicular to the wing surface.

Reynolds number. Figure visualizes the vortex structures using surfaces of constant Q criterion and shows a significant change in the vortex structures with AR.

Increasing the AR results in the LEV structure evolving into dual vortices in a similar manner to that observed in § 3.1 for increasing Reynolds number. This can be seen in figure by the splitting of the iso-Q surface near the leading edge into two co-rotating vortices and the formation of a secondary counter-rotating vortex as AR is increased. The development of the dual LEV system is also seen in the time-averaged contours of spanwise vorticity at 50 % span shown in figure . Here the same changes in flow patterns are observed with AR as was observed to occur with Reynolds number, namely the splitting of the negative vorticity region into two distinct vortex cores, an increase in strength of vorticity within the core of the downstream vortex and the formation of a region of positive vorticity between the two co-rotating vortex cores.

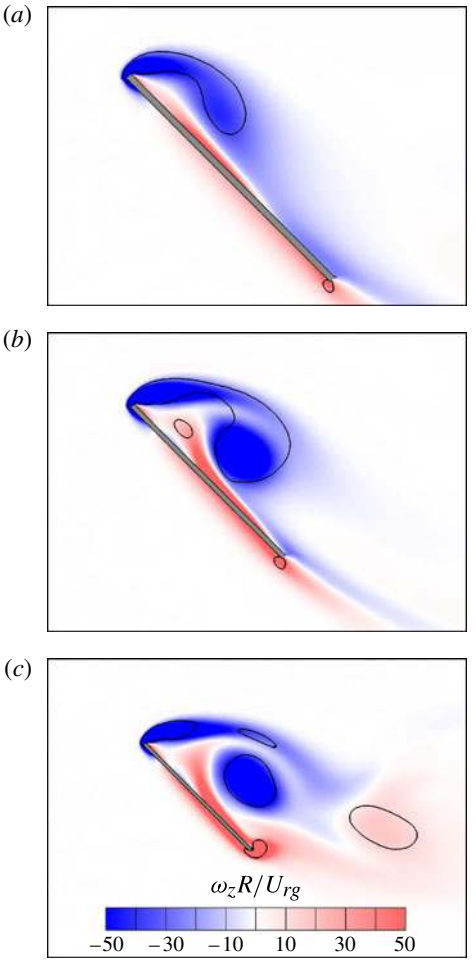

FIGURE 11. (Colour online) Contours of time-averaged spanwise vorticity ($\omega_z R/U_{rg}$) at 50 % span for wings at $Re = 300$: (*a*) $AR = 2.91$; (*b*) $AR = 5.1$; and (*c*) $AR = 7.28$. Solid lines are contours of constant Q criterion. Flow field has been averaged over the quasi-steady period ($0.36 \leqslant t/T \leqslant 1.0$).

In addition to the formation of dual LEVs, higher AR wings have larger LEVs in proportion to the wing chord. Consequently, the trailing edge of the wing is closer to the core of the downstream vortex (LEV 2) and this appears to result in the LEV interacting with the vorticity from the underside of the wing and the generation of unsteady vortex shedding out near the tip of the wing. This can be seen in figure by the increase in complexity of the vortex structures in the wake with AR. A more detailed discussion of this effect of AR is presented in § 3.4.2.

3.4. *Wing span as a characteristic length*

The striking similarity between the change in flow structures with AR and those with Reynolds number indicates that the two sets of results are linked, and may be scaled in an alternative manner so as to yield similar vortex structures for a range of aspect ratios. Figure gives a clue as to how these results may be scaled differently. Figure

shows the spanwise velocity that exists both within the core of the LEV and in the region immediately behind the wing. This velocity component dominates in this region and allows the LEV to grow in size (figure) and strength (figure *b*) along the span of the wing by convecting vorticity towards the wing tip (Maxworthy ; Ellington *et al.* ; Lentink & Dickinson). Hence, the key characteristic of the wing shape seems to be the wing span and not the wing chord.

We therefore propose the hypothesis that the wing span is a more useful characteristic length to use in the scaling of flapping and rotating wings at high angles of attack. In order to test this hypothesis we first non-dimensionalize the Navier–Stokes equation (3.3) using the method outlined by Lentink & Dickinson (),

$$\rho\frac{\mathrm{D}\boldsymbol{u}}{\mathrm{D}t}+\rho\dot{\boldsymbol{\Omega}}\times\boldsymbol{r}+\rho\boldsymbol{\Omega}\times(\boldsymbol{\Omega}\times\boldsymbol{r})+\rho 2\boldsymbol{\Omega}\times\boldsymbol{u}=-\nabla p+\mu\nabla^2\boldsymbol{u}. \tag{3.3}$$

Here we use the same scaling parameters as Lentink & Dickinson () except that we replace the average wing chord (c) with the wing span (R) as the characteristic length, thus the scaled variables become:

$$\boldsymbol{u}^*=\frac{\boldsymbol{u}}{U_{tip}},\quad t^*=\frac{U_{tip}t}{R},\quad \nabla^*=R\cdot\nabla,\quad \dot{\boldsymbol{\Omega}}^*=\frac{\dot{\boldsymbol{\Omega}}}{\dot{\Omega}}, \tag{3.4a,b,c,d}$$

$$\boldsymbol{\Omega}^*=\frac{\boldsymbol{\Omega}}{\Omega},\quad \boldsymbol{r}^*=\frac{\boldsymbol{r}}{R},\quad p^*=\frac{p}{p_0}, \tag{3.4e,f,g}$$

where U_{tip} is the wing tip velocity, p_0 is the ambient pressure, $\dot{\boldsymbol{\Omega}}$ is the angular acceleration vector and $\dot{\Omega}$ is the time-averaged angular acceleration amplitude. Substituting (3.4) into (3.3) and normalizing it by $\rho U_{tip}^2/R$ results in the following dimensionless equation,

$$\begin{aligned}\frac{\mathrm{D}\boldsymbol{u}}{\mathrm{D}t}+\frac{\dot{\Omega}R^2}{U_{tip}^2}\dot{\boldsymbol{\Omega}}\times\boldsymbol{r}+\frac{\Omega^2R^2}{U_{tip}^2}\boldsymbol{\Omega}\times(\boldsymbol{\Omega}\times\boldsymbol{r})+\frac{\Omega R}{U_{tip}}2\boldsymbol{\Omega}\times\boldsymbol{u}\\ =-\frac{p_0}{\rho U_{tip}^2}\nabla p+\frac{\mu}{\rho U_{tip}R}\nabla^2\boldsymbol{u},\end{aligned} \tag{3.5}$$

where * is omitted for clarity. Equation (3.5) shows that when the Navier–Stokes equation is scaled in this way, the Reynolds number becomes based on the wing span ($Re_R=\rho U_{tip}R/\mu$). Furthermore, the centripetal and Coriolis accelerations scale with $1/Ro^2$ and $1/Ro$, respectively, where $Ro=U_{tip}/\Omega R$ is the Rossby number. Lentink & Dickinson () propose that these rotational accelerations mediate LEV stability and, therefore, if this argument is true, then our new definition of Rossby number should describe LEV stability and the span-based Reynolds number should determine the structure of the LEV. The effects of these two parameters are investigated below.

3.4.1. *Scaling of results using a span-based Reynolds number*

Simulations of the fruit fly wing scaled to different aspect ratios were re-run with the fluid viscosity adjusted to match the span-based Reynolds number for each wing. The results of these tests were assessed to determine the dependence of the LEV structure on AR and span-based Reynolds number. Figure shows a comparison of the vortex structures over different AR wings for two span-based Reynolds numbers of 613 and 7667. These two Reynolds numbers are equivalent to $Re=120$ and 1500 for an AR of 2.91. Comparing the flow structures in this way shows a stronger correlation of the vortex structures between different AR wings at the same span-based

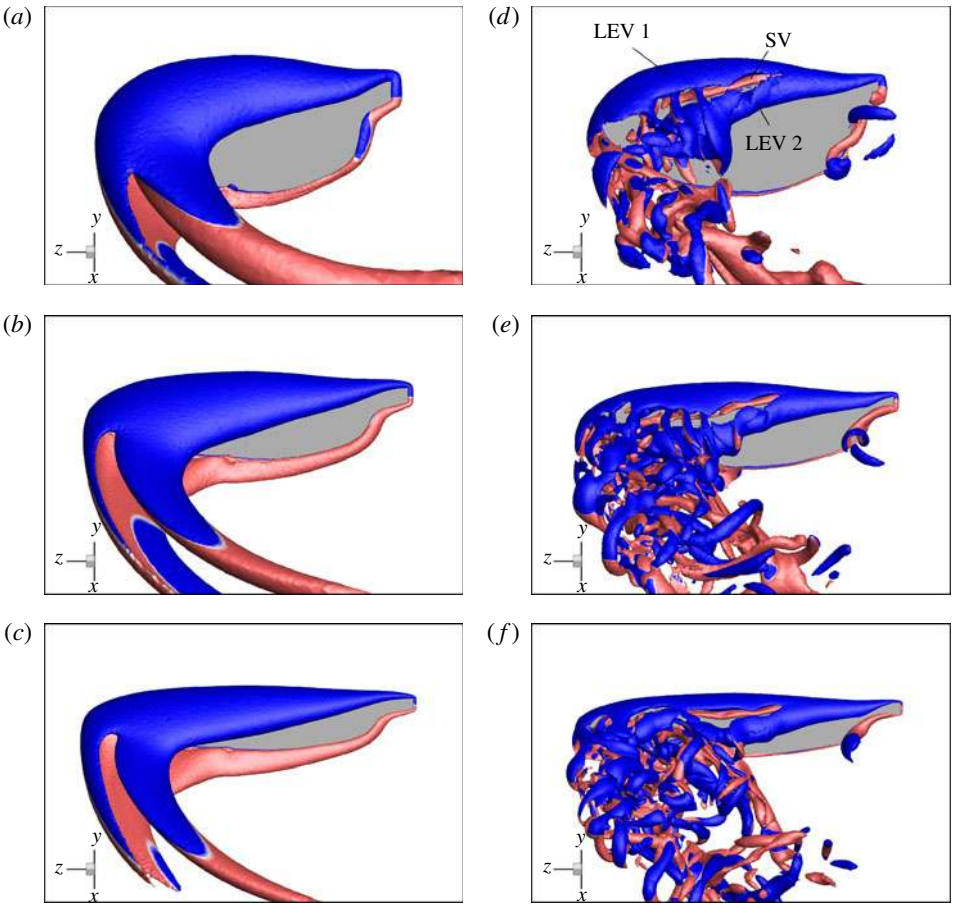

FIGURE 12. (Colour online) Vortex structures over different AR wings at span-based Reynolds numbers of (*a–c*) $Re_R = 613$ and (*d–f*) $Re_R = 7667$: (*a*,*d*) $AR = 2.91$; (*b*,*e*) $AR = 5.1$; (*c*,*f*) $AR = 7.28$. Vortex structures are visualized using surfaces of constant Q criterion and are coloured by spanwise vorticity (ω_z) to indicate direction; blue (dark grey) is negative and red (light grey) is positive. Images show the instantaneous flow structures at 270° of rotation and are taken perpendicular to the wing surface.

Reynolds number. For $Re_R = 613$ (figure 12*a–c*), all three wings show a very similar vortex structure. A single LEV extends along the wing until approximately 70 % span, where it separates and joins with the tip vortex. Similarly, the iso-Q surfaces for $Re_R = 7667$ (figure 12*d–f*) show similar vortex structures. Here the dual LEV structure is clearly evident and is well developed for all aspect ratios. Similar consistency in flow structures was found for intermediate span-based Reynolds numbers between 613 and 7667.

Sectional slices of spanwise vorticity further show the similarity of the LEV structure for the different AR wings when scaled with the span-based Reynolds number. At a span-based Reynolds number of 613 (figure 12*a–c*) all AR wings have a single region of strong negative vorticity located near the leading edge of the wing, while at a span-based Reynolds number of 7667 (figure 12*d–f*) the dual LEV structure

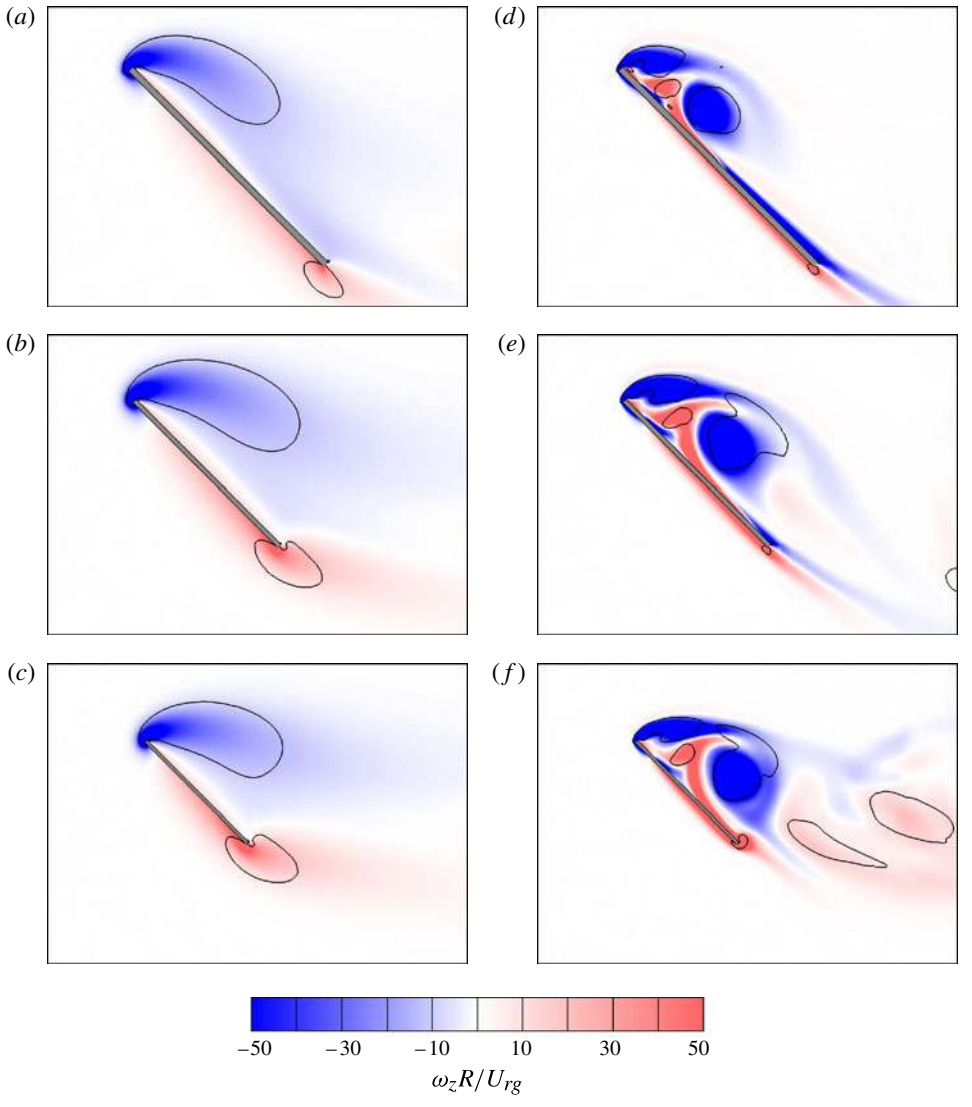

FIGURE 13. (Colour online) Contours of time averaged spanwise vorticity ($\omega_z R/U_{rg}$) at 50 % span for different AR wings at span-based Reynolds numbers of (*a–c*) $Re_R = 613$ and (*d–f*) $Re_R = 7667$: (*a*,*d*) $AR = 2.91$; (*b*,*e*) $AR = 5.1$; (*c*,*f*) $AR = 7.28$. Solid lines are contours of constant Q criterion. The flow field has been averaged over the quasi-steady period ($0.36 \leqslant t/T \leqslant 1.0$).

consisting of two regions of negative vorticity separated by a region of positive vorticity can be seen.

The spanwise position of the point at which the vortex core identification algorithm (Graftieaux *et al.*) recognizes two separate vortex cores is plotted against both the chord-based and span-based Reynolds numbers in figure . This shows that as the Reynolds number is increased the spanwise position at which two distinct vortex cores can be observed shifts towards the wing root. This can therefore be used as a measure of how much the dual LEV structure has developed for each wing. Figure (*a*) shows that the 'splitting' point depends on both the chord-based Reynolds number and the

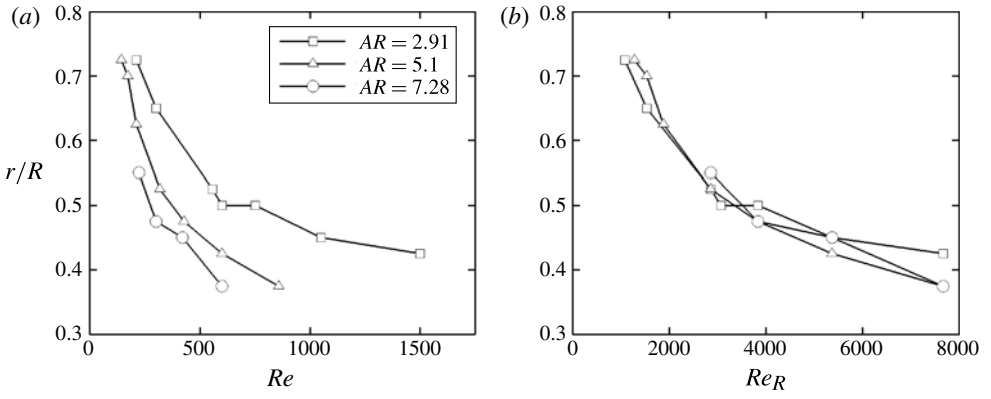

FIGURE 14. Normalized spanwise position (r/R) of the point at which two individual vortex cores are observed as a function of (*a*) Re and (*b*) Re_R.

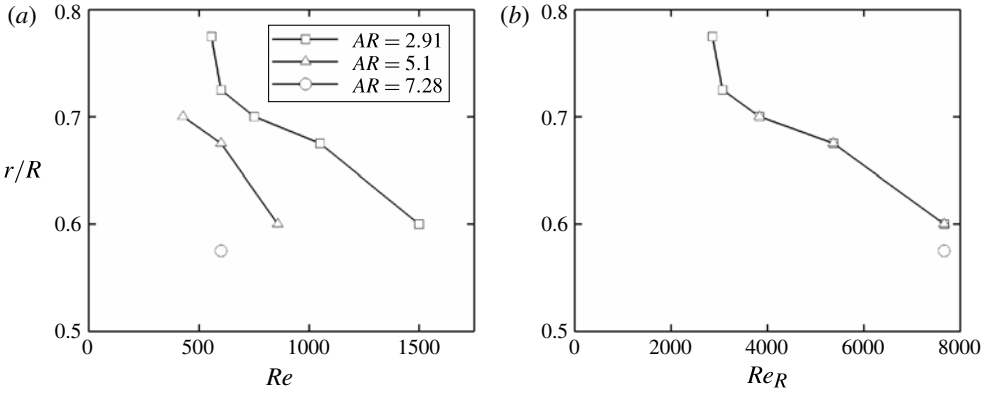

FIGURE 15. Normalized spanwise position (r/R) of the breakdown point of LEV 2 as a function of (*a*) Re and (*b*) Re_R.

wing AR. However, when these results are plotted against the span-based Reynolds number (figure *b*) the 'splitting' point becomes independent of the wing AR, as shown by the collapsing of the data onto effectively a single curve. This further demonstrates that the development of the dual LEV system is characterized by the span-based Reynolds number.

As shown in figure , at high Reynolds numbers LEV 2 breaks down at some point along the span. Vortex breakdown is an abrupt change in the structure of a vortex with a marked retardation of the flow in the axial direction (Hall). Figure shows the spanwise location of the breakdown point plotted against both the chord-based and span-based Reynolds numbers. Here, the breakdown point is estimated as the point at which the spanwise velocity in the vortex core approaches zero. Figure shows that as the Reynolds number is increased the burst point shifts towards the wing root and like the 'splitting' point, the spanwise position of the breakdown point can be described by the span-based Reynolds number for all aspect ratios.

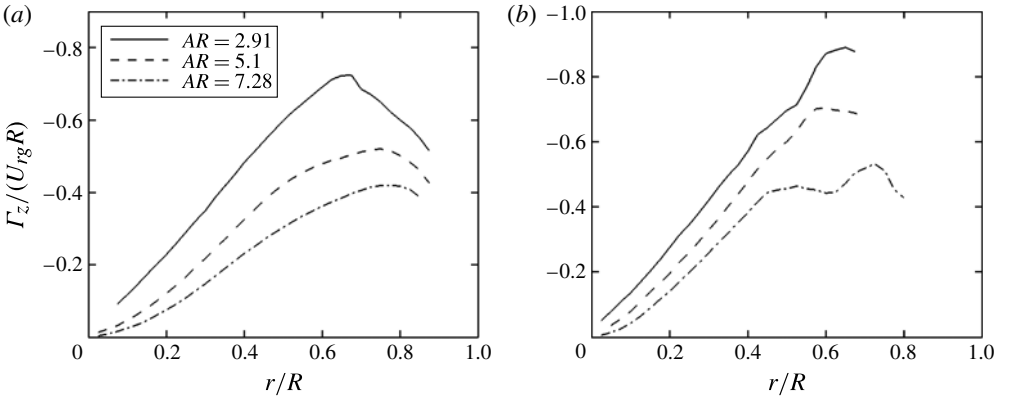

FIGURE 16. Combined circulation ($\Gamma_z/U_{rg}R$) of dual co-rotating LEVs for different AR wings at (*a*) $Re_R = 613$ and (*b*) $Re_R = 3833$. Note that only one vortex is present for $Re_R = 613$.

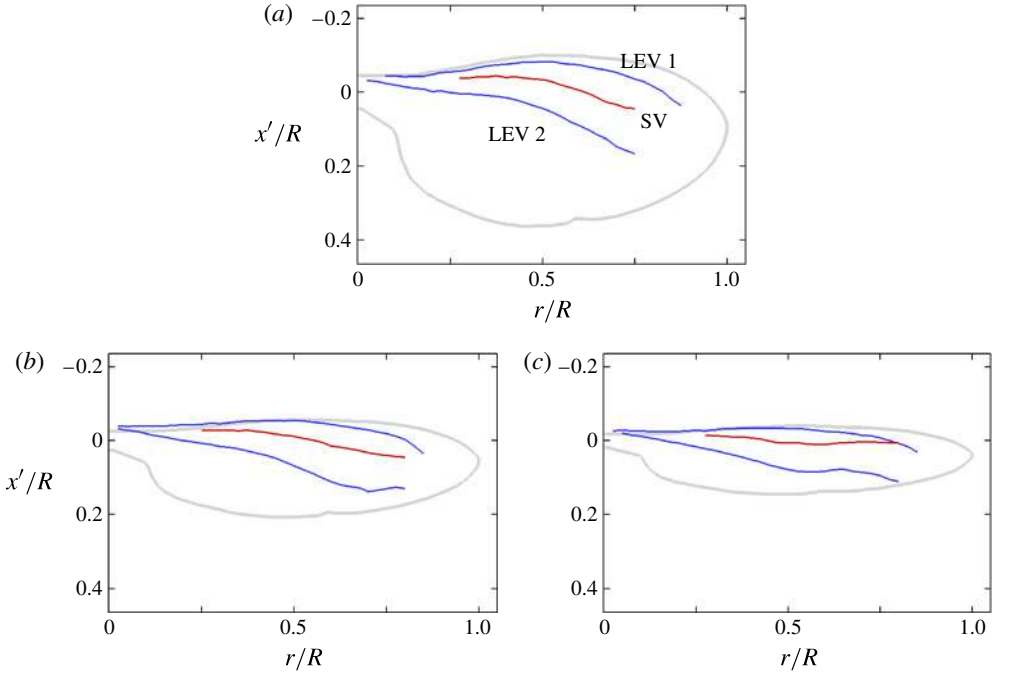

FIGURE 17. (Colour online) Vortex lines plotted in wing coordinates for aspect ratios of (*a*) 2.91, (*b*) 5.1 and (*c*) 7.28.

3.4.2. *Effect of AR at constant span-based Reynolds number*

Our results show that the span-based Reynolds number does indeed describe the structure of the LEV. Viewing the results in this way also allows the influence of AR and Reynolds number on the flow structure to be separated. The effect of wing AR on the flow structures is discussed below.

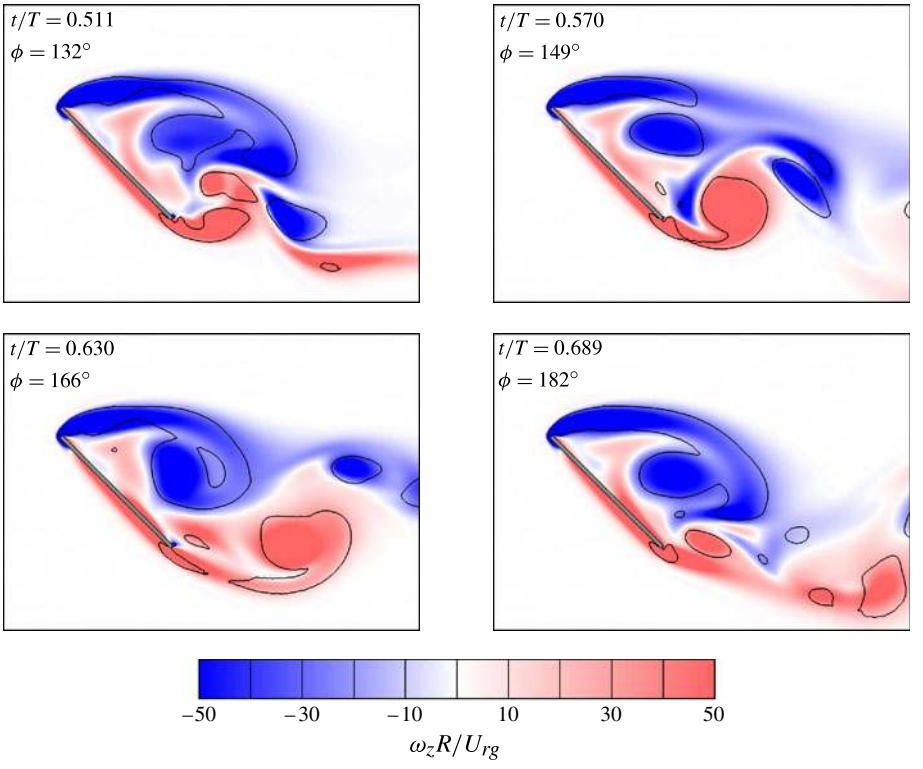

FIGURE 18. (Colour online) Time sequence of spanwise vorticity ($\omega_z R/U_{rg}$) at 70 % span for $AR = 7.28$ and $Re_R = 3833$. Solid lines are contours of constant Q criterion.

Figures ⌜ and ⌜ show that as the wing AR is increased the LEV increases in size relative to the chord length of the wing. At low span-based Reynolds numbers, when only LEV 1 is present, this does not have a significant impact on the structure of the LEV, however the circulation of the LEV is reduced for higher aspect ratios (figure ⌜ a). At higher Reynolds numbers, when the dual LEV structure is present, the position of LEV 2 is influenced by its proximity to the trailing edge. This can be seen in figure ⌜ which shows the vortex centrelines for the LEVs at three aspect ratios. For high-AR wings LEV 2 tracks across the wing moving away from the leading edge over the inner part of the wing but is deflected towards the tip when it reaches the trailing edge. For the $AR = 7.28$ wing this occurs around mid-span. After LEV 2 has been deflected it follows the trailing edge of the wing until it separates from the wing near the tip.

For high aspect ratios, the proximity of LEV 2 to the trailing edge causes LEV 2 to interact with the vorticity from the underside of the wing, which results in a region of unsteady flow to develop in the outer part of the wing, even before LEV 2 has burst. In fact this interaction seems to suppress the breakdown of LEV 2 as will be discussed later. An example of when this occurs is for the $AR = 7.28$ wing at a span-based Reynolds number of 3833. The instantaneous surfaces of the Q criterion at 270° of rotation are shown in figure ⌜ (c). This figure shows that the vortex structures are steady over the inner part of the wing, however beyond approximately 50 % span the flow becomes unsteady as indicated by the complex vortex structures in

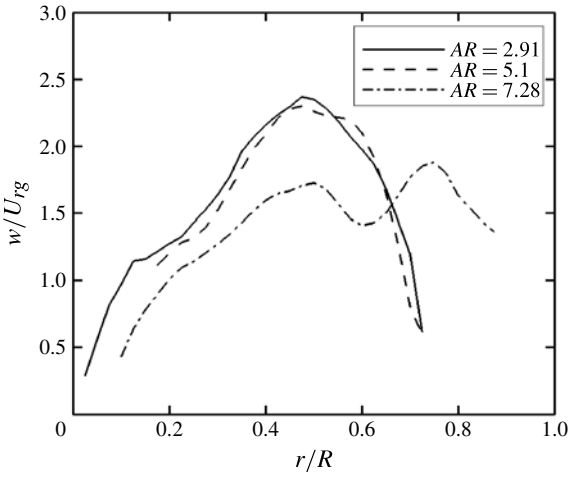

FIGURE 19. Spanwise velocity (w/U_{rg}) along the axis of LEV 2 at $Re_R = 3833$.

the wake. It is over this same region of the wing where LEV 2 follows the trailing edge (figure c). To show the fluctuation of the flow out near the wing tip more clearly the time evolution of the spanwise vorticity at 70 % span for the $AR = 7.28$ wing at $Re_R = 3833$ is shown in figure . Here, the proximity of LEV 2 to the trailing edge causes the vorticity from the underside of the wing to roll up into a trailing-edge vortex which is later shed from the wing. LEV 2 also appears to be pushed up slightly towards the leading edge and therefore interacts with the vorticity from the leading edge in a similar manner, resulting in negative sign vortices being shed from the wing. This continual interaction results in unsteady fluctuation of the flow in the outer part of the wing. Nonetheless, the dual LEV structure can always be visualized in figure . The LEV is therefore not completely shed as it would be for a purely translating high-aspect-ratio wing, and remains attached to the wing throughout the wing's rotation. The LEV does, however, have reduced circulation in this section of the wing as is shown in figure (*b*).

The interaction between LEV 2 and the vorticity at the trailing edge also appears to suppress the breakdown of LEV 2. Figure shows the spanwise velocity along the vortex axis at $Re_R = 3833$. At low aspect ratios, where LEV 2 is not influenced by the trailing edge, the spanwise flow in the vortex rapidly drops towards zero beyond the mid-span, which indicates the formation of a stagnation point and the beginning of vortex breakdown (Hall ; Leibovich). However at $AR = 7.28$ the peak in spanwise velocity in the vortex core is reduced and beyond 50 % span, where LEV 2 is following the trailing edge of the wing, the spanwise velocity fluctuates around a mean value and does not rapidly drop towards zero. This results in the suppression of the breakdown of LEV 2 for high aspect ratios at moderate span-based Reynolds numbers. When the Reynolds number is high enough such that the breakdown location occurs at or before the point that LEV 2 meets the trailing edge then LEV still undergoes vortex breakdown. This is the case for the $AR = 7.28$ wing at a span-base Reynolds number of 7667 as shown in figure (*f*).

Even though LEV 2 does not break down for high-*AR* wings at moderate span-based Reynolds numbers, this does not result in higher aerodynamic forces. In fact, the breakdown of LEV 2 does not seem to affect the lift coefficient greatly at any *AR*,

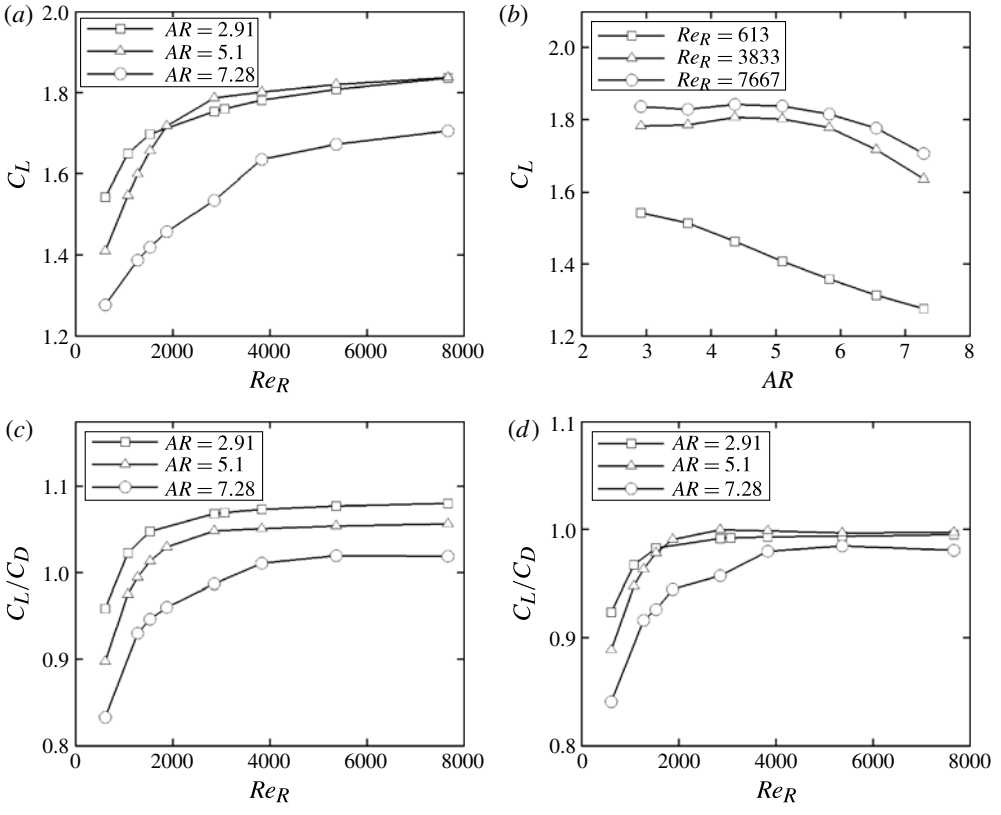

FIGURE 20. Aerodynamic force graphs: (*a*) average lift coefficient as a function of Re_R; (*b*) lift coefficient as a function of AR for three span-based Reynolds numbers; (*c*) average lift-to-drag ratio as a function of Re_R; and (*d*) lift-to-drag ratio ignoring wing thickness effects. Aerodynamic forces have been averaged over the quasi-steady period ($0.36 \leqslant t/T \leqslant 1.0$).

as shown in figure (*a*) by the approximately constant or slightly increasing lift coefficients for Reynolds numbers above 3000 where vortex breakdown was observed to occur. Actually, the interaction of LEV 2 with the trailing-edge vorticity results in reduced LEV circulation and therefore lower lift coefficients for high aspect ratios. Figure (*b*) shows that for span-based Reynolds numbers of 3833 and 7667 the lift coefficient is fairly constant up to $AR \approx 5$, after which the reduction in LEV circulation near the wing tip begins to reduce the wing's lift.

Figure (*c*) shows the lift-to-drag ratio for three wings as a function of span-based Reynolds number. It shows that for higher span-based Reynolds numbers the lift-to-drag ratio exceeds one for all wings. This is due to the pressure acting across the thickness of the wing's leading edge. To highlight this, figure (*d*) shows the lift-to-drag ratio after this surface has been removed from the aerodynamic force calculation. This shows that when the wing's thickness is ignored the lift-to-drag ratios for each wing become approximately one for high span-based Reynolds numbers. Therefore, the variation in lift-to-drag ratio with AR shown in figure (*c*) at these Reynolds numbers is an artefact of the proportionally thinner wings for higher aspect ratios.

Lower span-based Reynolds numbers represent a different flow regime where only LEV 1 is present. Here, the increased viscosity results in reduced gradient of

circulation as a function of wing span for higher aspect ratios (figure *a*). This reduces the lift capacity across the whole wing and therefore lowers the lift coefficient for higher aspect ratios (e.g. figure *b*, $Re_R = 613$). At these Reynolds numbers the skin friction force on the wing is also significant and accounts for between 4 and 8.5 % of the total lift and drag forces depending on the wing *AR*. Higher-*AR* wings have proportionally higher skin friction drag and therefore the lift-to-drag ratio is also reduced for increased aspect ratios.

3.4.3. *Discussion of LEV stability*

The ability for the LEV to remain attached to the wing is a key characteristic that is required in order to maintain high lift throughout the wing stroke. Studies that have investigated 2D and 3D translating wings at insect Reynolds numbers and high angles of attack have shown that the LEV is shed after a few chord lengths of travel (Dickinson & Gotz ; Miller & Peskin ; Taira & Colonius). However, studies that have incorporated the rotation of the wing about its base have often found stable LEVs (Usherwood & Ellington ; Birch *et al.* ; Lentink & Dickinson). One notable exception to this is that Jones & Babinsky (,) did not observe an attached LEV in their semi-submerged rotating wing experiments. Lentink & Dickinson ( ) have proposed that the centripetal and Coriolis accelerations due to wing rotation mediate LEV stability. In their analysis, these accelerations scale with the inverse of the Rossby number and therefore they suggest that low Rossby numbers, of the order of one, are required for the LEV to be stable.

As shown in § 3.4, our scaling of the Navier–Stokes equation using wing span resulted in the Rossby number being $Ro = U_{tip}/\Omega R$, and for the centripetal and Coriolis accelerations to scale with $1/Ro^2$ and $1/Ro$, respectively. For a hovering wing, where $U_{tip} = \Omega R$, this results in a Rossby number of one, which indicates that a stable LEV is always possible under this flight regime. Furthermore, letting $U_{tip} = U_\infty + \Omega R$, where U_∞ is the flight velocity of the insect or MAV, results in $Ro = U_\infty/\Omega R + 1$. This suggests that only large flight speeds compared with the velocity due to rotation would result in high Rossby numbers and therefore an unstable LEV. This condition is not tested here, however the stability of the LEV under hovering-type conditions is.

All of our simulations show that the LEV remains attached to the wing when it is rotating at a constant rotational velocity. We use the words ‘stable’ and ‘attached’ interchangeably to mean that the structure is persistent throughout the wing’s rotation and is not completely shed as it would be for a purely translating wing. At low span-based Reynolds numbers only LEV 1 is present and it remains attached to the wing for the majority of the span for all aspect ratios, only separating near the tip as it joins with the tip vortex (see figure *a–c*). At higher Reynolds numbers when the dual LEV structure is present, LEV 1 still remains attached to the wing’s leading edge despite the flow becoming unsteady out near the tip of the wing (figure *d–f*). LEV 2 also remains attached to the wing up until the point at which it bursts (figure *d–f*). Even at high aspect ratios and moderate Reynolds numbers, when the interaction between LEV 2 and the vorticity at the leading and trailing edges results in unsteady flow and vortex shedding, the dual LEV structure remains attached to the wing.

The finding that the LEV is always stable regardless of the aspect ratio or span-based Reynolds number agrees with the idea that the centripetal and Coriolis accelerations mediate LEV stability as the Rossby number is one for all our simulations. However, further investigation is required to confirm the behaviour of the LEV under forward flight conditions.

3.4.4. *Conditions for which span-based scaling is applicable*

Our results have shown that by using the wing's span rather than chord to scale the flow around a rotating wing allows the LEV structure to be characterized by a span-based Reynolds number. This scaling is useful when comparing the performance of wings with different planform shapes, as it allows each wing to have a comparable LEV structure. However, under what conditions is this scaling applicable? As explained above, this scaling comes about due to the strong spanwise velocity that dominates in the region immediately behind the wing, which allows the LEV to grow along the span. Therefore, the presence of a spanwise flow is a necessary condition in order for this scaling to be applied.

The spanwise pressure gradient that results from the wing's rotation and the centripetal and Coriolis rotational accelerations are both mechanisms which have been suggested to drive the spanwise velocity (Ellington *et al.* ; Aono *et al.* ; Lentink & Dickinson). Clearly the wing's rotation is important for both mechanisms. Lentink & Dickinson ( ) have proposed that moving the wing further away from its rotation axis is analogous to transitioning from pure rotation to only translation. It is therefore possible that increasing the offset distance will reduce the spanwise velocity compared to free stream velocity, which would be equivalent to increasing forward flight speed for a wing rotating about its base. Hence, the use of wing span as the characteristic length is likely to not apply for wings with large offset distances or large forward flight velocities. Another way of viewing this is simply that the span-based scaling may not apply when the Rossby number is high, as it is a measure of the wing's rotation compared with translation.

The strength of the spanwise velocity also seems to be linked to the wing's angle of attack. Usherwood & Ellington ( ) observed for their rotating model hawkmoth wings that at very low angles of attack there was no spanwise flow. Occasionally at small angles of attack, around 10°, the flow separated from the leading edge and travelled rapidly towards the tip and only at higher angles of attack did a consistent spanwise velocity form. Lu *et al.* ( ) also noted that considerable spanwise flows were only generated for angles of attack above 30°. Finally, for angles of attack greater than 30°, Ozen & Rockwell ( ) observed increasing maximum spanwise velocities with angle of attack. Consequently, it is possible that the wing's angle of attack also plays a role in determining when the span-based scaling can apply.

Many studies in the literature that have observed stable LEVs have reported a 3D LEV structure along the wing's span as well as significant spanwise flows on the leeward side of the wing. In addition, the simplified kinematic motion used in this study has been shown to be a good approximation of the beginning of a typical insect's flapping stroke (Poelma *et al.* ; Lentink & Dickinson) and thus generates similar structures to those seen on flapping wings. Therefore, this span-based scaling has the potential to apply over a wide range of both flapping and rotating wing flows. The above discussion suggests that the wing's offset from it's rotation axis, angle of attack and flight velocity may all have an influence on when this scaling can apply, however, the extent to which these parameters influence this requires further investigation.

3.5. *Prediction of vortex breakdown*

In the past, several vortex breakdown criteria have been applied to both free swirling jets and swirling pipe flows in order to predict the onset of vortex breakdown. In this section we attempt to apply one of these criteria to our data to see whether it can successfully predict vortex breakdown in a more complex flow. Here we use

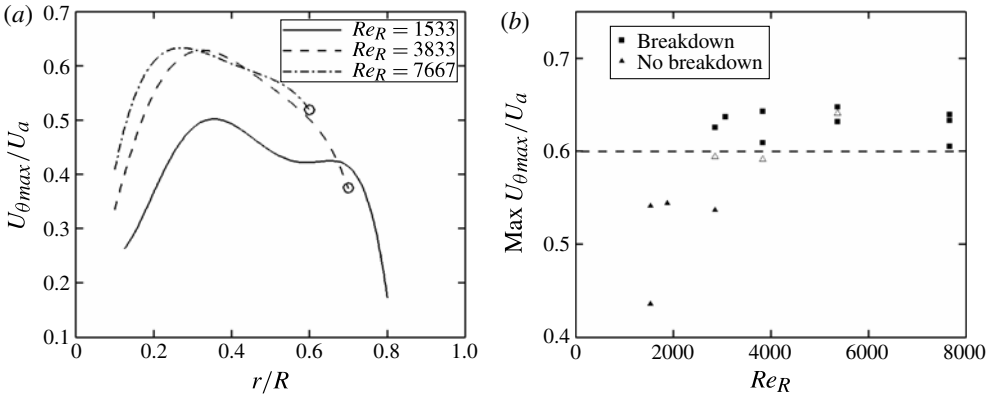

FIGURE 21. Swirl parameter graphs. (*a*) Variation of the swirl parameter along the wing's span for the $AR = 2.91$ wing at three Re_R values. Open circles indicate the spanwise position of the breakdown point. (*b*) Maximum swirl parameter as a function of Re_R. Open symbols represent high-*AR* cases where vortex breakdown is suppressed due to the proximity of LEV 2 to the trailing edge.

the swirl parameter proposed by Billant, Chomaz & Huerre ( ). They derive the vortex breakdown criterion by considering the case of a free vortex undergoing conical breakdown in a flow of infinite extent. The Bernoulli equation is applied along the streamline on the vortex axis and the assumption is made that the stagnation region is directly connected to the surrounding quiescent fluid and therefore the pressure at stagnation is equal to the ambient pressure. This results in the following relation

$$\frac{\displaystyle\int_0^\infty \frac{U_\theta^2}{l}\,\mathrm{d}l}{U_a^2} = \frac{1}{2}, \tag{3.6}$$

where U_a is the axial velocity on the vortex axis, U_θ is the azimuthal velocity and l is the radial distance from the vortex axis. To simplify this further the particular case of a Rankine vortex is considered. Here, $U_\theta = \Omega_\theta l$ within the vortex core ($l \leqslant a$) and $U_\theta = \Omega_\theta a^2/l$ outside it ($l > a$), where Ω_θ is the solid body rotational velocity of the vortex. Thus, this criterion reduces to

$$\frac{U_{\theta max}}{U_a} = \frac{1}{\sqrt{2}}, \tag{3.7}$$

where $U_{\theta max}$ is the maximum azimuthal velocity.

This swirl criterion is applied to LEV 2 in figure (*a*), which shows the variation of this parameter along the span for the $AR = 2.91$ wing at three span-based Reynolds numbers. For high span-based Reynolds numbers where LEV 2 is observed to break down, the swirl parameter rapidly increases near the root of the wing and reaches a maximum value before reducing more slowly with span until the point of breakdown (as indicated by the open circles). For these Reynolds numbers, the maximum swirl criterion that is reached is of a comparable value. For the lowest span-based Reynolds number, vortex breakdown was not observed to occur and the swirl parameter is generally much lower across the whole span. Figure (*b*) shows a plot of the maximum swirl parameter with span-based Reynolds number applied to all cases

where a dual LEV system was observed over a portion of the wing. It shows that for all cases where vortex breakdown occurs the maximum swirl parameter exceeded a value of approximately 0.6, which suggests that this is the critical value for this flow regime. This critical value is, however, of the order of 15 % lower than the theoretical limit of $1/\sqrt{2}$. Nevertheless, the assumptions of an infinite flow extent and of the stagnation pressure being equal to the ambient pressure, which are made in the derivation of (3.7), do not apply to this flow regime and could account for the lower critical value. It is worth noting, however, that maximum swirl values of around 0.6 or higher were calculated for some cases but no vortex breakdown was seen to occur. These are shown in figure (*b*) by the open symbols and correspond to high aspect ratios where vortex breakdown is suppressed because of the interaction of LEV 2 with the trailing edge. Under these conditions the prediction of vortex breakdown failed and so the application of this breakdown criterion to our data was only partially successful.

4. Conclusion

In this paper we have investigated the flow structures over rotating wings with different aspect ratios for a range of Reynolds numbers. Simulations of a fruit fly wing ($AR = 2.91$) were conducted at Reynolds numbers between 120 and 1500. Over this Reynolds number range a dual LEV structure was found to develop, where the LEV split into two co-rotating vortex structures separated by a smaller counter-rotating vortex. Results at higher aspect ratios revealed that the same dual LEV structure develops with increasing *AR* at a fixed Reynolds number.

Analysis of the flow structures suggested that these results could be scaled in an alternative manner so as to decouple the effects of Reynolds number and *AR*. We found that by using the wing's span as the characteristic length, rather than chord, that these results could be scaled using a span-based Reynolds number to yield similar LEV structures for different *AR* wings. The span-based Reynolds number was able to independently describe the location where two co-rotating vortices could be observed as well as the breakdown point of the downstream vortex.

This scaling may prove to be useful when comparing the performance of different wing shapes and was used in this study to assess the impact of *AR* on the flow structures and aerodynamic forces. At low span-based Reynolds numbers higher-*AR* wings had reduced LEV circulation and therefore lift coefficients. At high span-based Reynolds numbers, when the dual LEV structure had developed, it was found that high-*AR* wings altered the direction of the downstream LEV near the wing tip. In this region the LEV follows the trailing-edge of the wing and interacts with the positive vorticity from underneath the wing, resulting in a region of unsteady flow in the outer part of the wing and suppression of vortex breakdown of the LEV. This interaction resulted in reduced LEV circulation and lower lift coefficients for high-*AR* wings. This finding shows that low-*AR* wings do in fact outperform high-*AR* wings under these conditions.

The limitations of using wing span as a characteristic length were assessed and determined to be restricted to flapping and rotating wings revolving about their base at high angles of attack where a strong spanwise velocity dominates immediately behind the wing. These conditions are typical of those seen in nature, and hence this scaling could be applied to investigations involving insects and birds as well as nature-mimicking MAVs.

Acknowledgements

This research was undertaken with the assistance of resources provided at the Australian National University through the National Computational Merit Allocation Scheme supported by the Australian Government.

REFERENCES

ANSARI, S. A., KNOWLES, K. & ZBIKOWSKI, R. 2008 Insectlike flapping wings in the hover part 2: effect of wing geometry. *J. Aircraft* **45** (6), 1976–1990.

AONO, H., LIANG, F. & LIU, H. 2008 Near- and far-field aerodynamics in insect hovering flight: an integrated computational study. *J. Expl Biol.* **211**, 239–257.

BILLANT, P., CHOMAZ, J. M. & HUERRE, P. 1998 Experimental study of vortex breakdown in swirling jets. *J. Fluid Mech.* **376**, 183–219.

BIRCH, J. M. & DICKINSON, M. H. 2001 Spanwise flow and the attachment of the leading-edge vortex on insect wings. *Nature* **412**, 729–733.

BIRCH, J. M., DICKSON, W. B. & DICKINSON, M. H. 2004 Force production and flow structure of the leading edge vortex on flapping wings at high and low Reynolds numbers. *J. Expl Biol.* **207** (7), 1063–1072.

DICKINSON, M. H. & GOTZ, K. G. 1993 Unsteady aerodynamic performance of model wings at low Reynolds numbers. *J. Expl Biol.* **174** (1), 45–65.

DICKINSON, M. H., LEHMANN, F.-O. & SANE, S. P. 1999 Wing rotation and the aerodynamic basis of insect flight. *Science* **284**, 1954–1960.

ELLINGTON, C. P. 1984 The aerodynamics of hovering insect flight. II. Morphological parameters. *Phil. Trans. R. Soc.* B: *Biol. Sci.* **305** (1122), 17–40.

ELLINGTON, C. P., VAN DEN BERG, C., WILLMOTT, A. P. & THOMAS, A. L. R. 1996 Leading-edge vortices in insect flight. *Nature* **384** (19), 626–630.

GRAFTIEAUX, L., MICHARD, M. & GROSJEAN, N. 2001 Combining PIV, POD and vortex identification algorithms for the study of unsteady turbulent swirling flows. *Meas. Sci. Technol.* **12**, 1422–1429.

HALL, M. G. 1972 Vortex breakdown. *Annu. Rev. Fluid Mech.* **4** (1), 195–218.

HUNT, J. C. R., WRAY, A. A. & MOIN, P. 1988 Eddies, streams, and convergence zones in turbulent flows. *Tech. Rep.* CTR-S88. Center for Turbulence Research.

JONES, A. R. & BABINSKY, H. 2010 Unsteady lift generation on rotating wings at low Reynolds numbers. *J. Aircraft* **47** (3), 1013–1021.

JONES, A. R. & BABINSKY, H. 2011 Reynolds number effects on leading edge vortex development on a waving wing. *Exp. Fluids* **51** (1), 197–210.

KWEON, J. & CHOI, H. 2010 Sectional lift coefficient of a flapping wing in hovering motion. *Phys. Fluids* **22** (7).

LEIBOVICH, S. 1978 The structure of vortex breakdown. *Annu. Rev. Fluid Mech.* **10**, 221–246.

LENTINK, D. & DICKINSON, M. H. 2009*a* Biofluiddynamic scaling of flapping, spinning and translating fins and wings. *J. Expl Biol.* **212** (16), 2691–2704.

LENTINK, D. & DICKINSON, M. H. 2009*b* Rotational accelerations stabilize leading edge vortices on revolving fly wings. *J. Expl Biol.* **212** (16), 2705–2719.

LIU, H. & AONO, H. 2009 Size effects on insect hovering aerodynamics: an integrated computational study. *Bioinspir. Biomimet.* **4**.

LU, Y., SHEN, G. X. & LAI, G. J. 2006 Dual leading-edge vortices on flapping wings. *J. Expl Biol.* **209**, 5005–5016.

LUO, G. & SUN, M. 2005 The effects of corrugation and wing planform on the aerodynamic force production of sweeping model insect wings. *Acta Mechanica Sin.* **21** (6), 531–541.

MAXWORTHY, T. 1979 Experiments on the Weis–Fogh mechanism of lift generation by insects in hovering flight. Part 1. Dynamics of the fling. *J. Fluid Mech.* **93** (01), 47–63.

MILLER, L. A. & PESKIN, C. S. 2004 When vortices stick: an aerodynamic transition in tiny insect flight. *J. Expl Biol.* **207**, 3073–3088.

OZEN, C. A. & ROCKWELL, D. 2011 Flow structure on a rotating plate. *Exp. Fluids* **52**, 207–223.

PHILLIPS, N., KNOWLES, K. & LAWSON, N. J. 2010 Effect of wing planform shape on the flow structures of an insect-like flapping wing in Hover. In *27th International Congress of the Aeronautical Sciences*. ICAS.

PINES, D. J. & BOHORQUEZ, F. 2006 Challenges facing future micro-air-vehicle development. *J. Aircraft* **43** (2), 290–305.

POELMA, C., DICKSON, W. B. & DICKINSON, M. H. 2006 Time-resolved reconstruction of the full velocity field around a dynamically-scaled flapping wing. *Exp. Fluids* **41** (2), 213–225.

ROACHE, P. J. 1998 Verification of codes and calculations. *AIAA J.* **36** (5), 696–702.

SHYY, W., AONO, H., CHIMAKURTHI, S. K., TRIZILA, P., KANG, C.-K., CESNIK, C. E. S. & LIU, H. 2010 Recent progress in flapping wing aerodynamics and aeroelasticity. *Prog. Aeronaut. Sci.* **46** (7), 284–327.

SRYGLEY, R. B. & THOMAS, A. L. R. 2002 Unconventional lift-generating mechanisms in free-flying butterflies. *Nature* **420**, 660–664.

TAIRA, K. & COLONIUS, T. 2009 Three-dimensional flows around low-aspect-ratio flat-plate wings at low Reynolds numbers. *J. Fluid Mech.* **623**, 187–207.

TSUZUKI, N., SATO, S. & ABE, T. 2007 Design guidelines of rotary wings in hover for insect-scale micro air vehicle applications. *J. Aircraft* **44** (1), 252–263.

USHERWOOD, J. R. & ELLINGTON, C. P. 2002*a* The aerodynamics of revolving wings I. Model hawkmoth wings. *J. Expl Biol.* **205** (11), 1547–1564.

USHERWOOD, J. R. & ELLINGTON, C. P. 2002*b* The aerodynamics of revolving wings II. Propeller force coefficients from mayfly to quail. *J. Expl Biol.* **205** (11), 1565–1576.

WALKER, J. D. A., SMITH, C. R., CERRA, A. W. & DOLIGALSKI, T. L. 1987 The impact of a vortex ring on a wall. *J. Fluid Mech.* **181**, 99–140.

ZANKER, J. M. & GOTZ, K. G. 1990 The wing beat of drosophila melanogaster. II. Dynamics. *Phil. Trans. R. Soc.* B: *Biol. Sci.* **327**, 19–44.